The molecular polar disc in NGC 2768

Alison F. Crocker, Martin Bureau, Lisa M. Young, Françoise Combes

Mon. Not. R. Astron. Soc. **386,** 1811–1820 (2008) doi:10.1111/j.1365-2966.2008.13177.x

The molecular polar disc in NGC 2768⋆

Alison F. Crocker,[1]† Martin Bureau,[1] Lisa M. Young[1,2] and Francoise Combes[3]

[1]*Sub-Department of Astrophysics, University of Oxford, Denys Wilkinson Building, Keble Road, Oxford OX1 3RH*
[2]*Department of Physics, New Mexico Institute of Mining and Technology, Socorro, NM 87801, USA*
[3]*Observatoire de Paris, LERMA, 61 Av. de l'Observatoire, 75014, Paris, France*

Accepted 2008 February 28. Received 2008 February 25; in original form 2007 November 26

ABSTRACT

We present CO(1–0) and CO(2–1) maps of the molecular polar disc in the elliptical galaxy NGC 2768 obtained at the Institute de Radioastronomie Millimétrique (IRAM) Plateau de Bure Interferometer. The maps have a resolution of $2\farcs6 \times 2\farcs3$ and $1\farcs2 \times 1\farcs2$ for the CO(1–0) and CO(2–1) lines, respectively. The CO maps complete the unique picture of the interstellar medium (ISM) of NGC 2768; the dust, molecular gas, ionized gas and neutral hydrogen (H I) trace the recent acquisition of cold and cool gas over two orders of magnitude in radii (and much more in density). In agreement with the other ISM components, the CO distribution extends nearly perpendicularly to the photometric major axis of the galaxy. Velocity maps of the CO show a rotating polar disc or ring in the inner kiloparsec. This cool gas could lead to kinematic substructure formation within NGC 2768. However, the stellar velocity field and Hβ absorption line-strength maps from the optical integral-field spectrograph SAURON give no indication of a young and dynamically cold stellar population coincident with the molecular polar disc. Very recent or weak star formation, undetectable in line strengths, nevertheless remains a possibility and could be at the origin of some of the ionized gas observed. Millimetre continuum emission was also detected in NGC 2768, now one of only a few low-luminosity active galactic nuclei with observed mm continuum emission.

Key words: galaxies: elliptical and lenticular, cD – galaxies: evolution – galaxies: individual: NGC 2768 – galaxies: ISM – galaxies: kinematics and dynamics – galaxies: structure.

1 INTRODUCTION

Galaxy formation scenarios must explain the rather uniform global properties of early-type galaxies as seen in the fundamental plane (e.g. Djorgovski & Davis 1987; Dressler et al. 1987) while simultaneously accounting for the diversity seen in the internal kinematics and stellar populations (e.g. de Zeeuw et al. 2002). Indeed, the maps of the stellar kinematics of 48 elliptical (E) and S0 galaxies from the SAURON optical integral-field unit (IFU) have shown a wide variety of kinematic substructures from large embedded discs to small counter-rotating cores (e.g. Emsellem et al. 2004; McDermid et al. 2006). Major mergers have been found to reproduce many of the kinematic substructures observed in the SAURON maps without invoking post-merger star formation (Jesseit et al. 2007). However, many of the kinematically decoupled components (KDCs) in the SAURON maps are very young (Kuntschner et al. 2006; McDermid et al. 2006), suggesting their stars formed *in situ*, and not as part of another galaxy.

Over the past 20 yr, it has been shown that E/S0s do have detectable amounts of cool and cold gas. Cold dust was first found in the *IRAS* survey in which around 45 per cent of ellipticals were detected in both the 60 and 100 μm bands (Knapp at al. 1989). Molecular gas detections have often been biased towards dust-rich or infrared-bright galaxies, but two recent surveys do not select on these criteria and give detection rates of 28 per cent for E/S0s in the SAURON representative sample (Combes, Young & Bureau 2007) and 78 per cent for S0s in a volume-limited sample (Sage & Welch 2006). Particularly interesting for substructure formation are the maps of cold molecular gas provided by interferometric CO observations (e.g. Young 2002, 2005). These maps often show rotating molecular gas discs on the same spatial scales as KDCs.

While the current evidence indirectly connects molecular gas discs with young KDCs, the details of the connection are still unknown. Do all molecular discs form stellar components? Do stars form everywhere in the molecular disc, or only in the densest regions? Does the regularity of the morphology of the molecular disc (presumably indicating how long since the gas was accreted) correlate with the age of the stars? To answer these questions, we must compare the molecular gas morphology and kinematics to the stellar

⋆Based on observations carried out with the IRAM Plateau de Bure Interferometer. IRAM is supported by INSU/CNRS (France), MPG (Germany) and IGN (Spain).
†E-mail: afc@astro.ox.ac.uk

morphology, kinematics and ages in a spatially resolved manner. This comparison requires interferometric CO maps and optical (or near-infrared) IFU data for many individual galaxies. With this comparison in mind, we have started to obtain CO synthesis maps for the 12 early-type SAURON galaxies recently detected in CO (see Combes et al. 2007, and references therein).

In this paper, we present the first CO synthesis maps of NGC 2768 and compare the molecular gas to the stellar and ionized gas properties from SAURON. NGC 2768 is classified as an E6 galaxy in RC3 (de Vaucouleurs et al. 1991), an S0 in the Carnegie Atlas of Galaxies (Sandage & Bedke 1994), and as a fast rotator in the recently proposed kinematic classification scheme of Emsellem et al. (2007). Kim (1989) first discovered both the polar orientation of the inner dust lane and the rotation of the ionized gas about the major axis, suggesting an external accretion origin for the dust and gas. NGC 2768 has a low-luminosity active galactic nucleus (AGN) with a low-ionization nuclear emission-line region (LINER) spectrum (Heckman 1980), a compact radio core (Nagar, Falcke & Wilson 2005) and an X-ray source consistent with being a point source (Komossa, Böhringer & Huchra 1999). General properties of NGC 2768 are listed in Table 1.

This paper is organized as follows. In Section 2, we describe the calibration and reduction of the data from the Plateau de Bure Interferometer. Section 3 presents flux measurements for the continuum data and channel maps, total intensity maps and velocity fields for the CO line data. In Section 4, we discuss the origin and fate of the molecular gas and also consider the contributions to the mm continuum flux from the low-luminosity AGN (LLAGN) and cold dust. We draw our conclusions in Section 5.

2 OBSERVATIONS AND DATA REDUCTION

We observed NGC 2768 in 2005 December (C configuration) and 2006 August (D configuration) at the IRAM Plateau de Bure Interferometer (PdBI). The ^{12}CO(1–0) and ^{12}CO(2–1) lines were observed simultaneously using dual-band SIS receivers. All six 15-m antennae were used for the C-configuration observations in December while only five antennae were available for the August observations. Typical system temperatures were 200–300 K for the CO(1–0) line in both months and the CO(2–1) in December. In the worse weather of August, the CO(2–1) line observations had system temperatures of 300–1000 K. The spectral correlators were centred at 114.743 and 229.482 GHz, the transition frequencies of CO(1–0) and CO(2–1) corrected for the galaxy's heliocentric velocity of 1373 km s^{-1}. The correlator configuration used four 160-MHz wide [417 and 209 km s^{-1} for CO(1–0) and CO(2–1), respectively] units with a frequency resolution of 1.25 MHz (3.3 and 1.6 km s^{-1}), covering a total bandwidth of 580 MHz (1670 and 835 km s^{-1}). The correlator was regularly calibrated by a noise source inserted in the internal frequency system.

Table 1. Basic properties of NGC 2768. The left-hand side and middle columns list the different quantities and their values; the right-hand side column lists corresponding references.

Quantity	Value	References
RA (J2000)	09 11 37.413	1
Dec. (J2000)	+60 02 14.86	1
Heliocentric velocity	1373 ± 5 km s^{-1}	2
Distance	21.5 Mpc	3
Scale	1 arcsec = 104 pc	3
Type (RC3)	E6	4
Type (CAG)	S0	5
Corrected apparent B mag	10.60	6
Corrected absolute B mag	−21.15	6
$L_{\rm B}$	2.3×10^{10} L$_\odot$	7
$L_{\rm FIR}$	4.3×10^{8} L$_\odot$	7
$L_{\rm FIR}/L_{\rm B}$	1.9×10^{-2}	7
$L_{\rm FIR}/M_{\rm H_2}$	6.3 L$_\odot$/M$_\odot$	7

References: (1) Nagar et al. (2005); (2) NED; (3) Emsellem et al. (2004); (4) de Vaucouleurs et al. (1991); (5) Sandage & Bedke (1994); (6) HYPERLEDA; (7) derived quantity using data from NED, *IRAS* (Moshir et al. 1990), and this paper.

We obtained visibilities with series of twenty 1 min integrations on source, followed by three 45-s phase and amplitude calibrations on a nearby quasar, 0836+710. As 08366+710 was not bright enough, we used 3C84 (December 20), 05286+134 (August 25) and MWC349 (August 28) as flux calibrators. Comparing the flux measured for 08366+710 on August 28 to that measured on December 25 suggests an uncertainty in our flux calibration of ≈20 per cent. This is unfortunately not a very good estimate as the true flux of 08366+710 may have varied over the 8-month interval.

The data were reduced with the Grenoble Image and Line Data Analysis System (GILDAS) software packages CLIC and MAPPING (Guilloteau & Lucas 2000). Using CLIC, we first calibrated the data using the standard pipeline. Data obtained during periods of bad weather were flagged and then ignored. After calibration, we used MAPPING to create two data cubes for both lines with velocity planes separated by 40 and 60 km s^{-1}. The primary beam size is 44 arcsec for the CO(1–0) observations and 22 arcsec for the CO(2–1) observations. We choose the spatial dimensions of the data cube to be twice the diameter of the primary beam, 88 × 88 and 44 × 44 arcsec^2 for the CO(1–0) and CO(2–1) lines, respectively. The synthesized beam sizes are 2.″6 × 2.″3 for CO(1–0) and 1.″2 × 1.″2 for CO(2–1). We thus choose spatial pixels of 0.7 × 0.7 and 0.35 × 0.35 arcsec^2 for the CO(1–0) and CO(2–1) lines, respectively. As we detected continuum emission, we subtracted the continuum using the task CONTSUB in the Multichannel Image Reconstruction, Image Analysis and Display (MIRIAD) software package (Sault, Teuben & Wright 1995). The dirty beam has small side lobes that necessitated cleaning the data cube. The cleaning was done using the Högbom method (Högbom 1974); we stopped cleaning in each velocity plane after the brightest residual pixel had a value lower than the rms of the uncleaned data cube.

To constrain the continuum emission, we selected channels at least 40 km s^{-1} away from the highest and lowest velocity channels with any line emission in the cleaned data cubes. The very edges of the 580-MHz bandwidth were also avoided. The resulting continuum windows were 356- and 200-MHz wide at 115 and 230 GHz, respectively. We used the MAPPING tasks with the same parameters as for the line data to create clean images of the continuum at both frequencies. We fit point-source models in the *uv* plane to find the flux of the 3-mm continuum and an upper limit for the 1-mm continuum. The continuum emission is spatially unresolved at both frequencies.

3 RESULTS

We detected extended emission in both the CO(1–0) and CO(2–1) lines and point-source continuum emission at 3 mm.

3.1 Continuum emission

The continuum maps at 1 and 3 mm, both show peaks at the centre of NGC 2768. The 3-mm continuum map has a peak of over 6σ

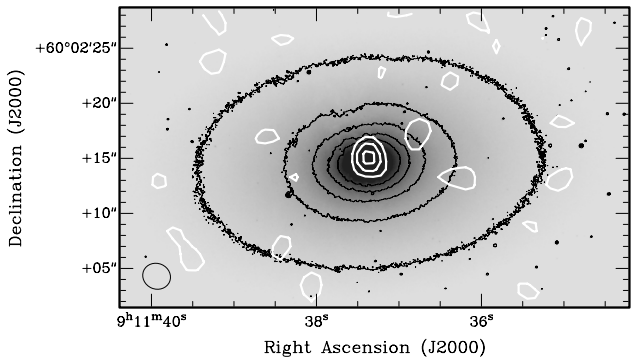

Figure 1. 3-mm continuum contours (white) over a *HST* Advanced Camera for Surveys (ACS) image (F814W filter, black contours) of NGC 2768. Contours are at 2, 4 and 6σ, where $\sigma = 0.28$ mJy beam^{-1}. The synthesized beam is plotted in the lower left-hand corner.

consistent with being a point source (see Fig. 1). Fitting a point-source model in the *uv*-plane yields a flux density of 1.94 mJy at a right ascension (RA) of 09 11 37.38 and declination (Dec.) of +60 02 14.8. This position is off the Very Large Array (VLA) coordinates of Nagar et al. (2005) by −0.5 arcsec in RA and −0.″1 in Dec. Given the 2.″6 × 2.″3 beam, this source is, however, still identifiable with the radio source, despite the large offset in RA. The 1-mm continuum map shows a weak peak at the same location. Fitting a point-source model in the *uv* plane to the same coordinates as found for the 3-mm continuum emission gives a flux density of 1.56 mJy with a rms noise $\sigma = 0.75$ mJy. We thus do not consider this a reliable determination of the flux density at 1 mm, and instead adopt a 3σ upper limit of 2.25 mJy.

3.2 CO line emission

Fig. 2 shows the channel maps for the CO(1–0) and CO(2–1) lines from the 60 km s^{-1} data cubes. To draw attention to the overall morphology and kinematics of the CO, we created integrated intensity maps, mean velocity field maps and position-velocity (PV) diagrams using the 40 km s^{-1} data cubes, for better velocity resolution (Figs 3 and 4). To make these maps, we first created a smoothed cube by smoothing with a 2D Gaussian [full width at half-maximum (FWHM) of 4 pixels] spatially and Hanning smoothing by three channels in velocity. We then computed the moments by integrating in velocity over the pixels in the original cube that corresponded to pixels above 3σ in the smoothed cube. As the emission is oriented primarily north–south, we created the PV diagrams by computing the zeroth moment of the masked cube in the declination-velocity plane. This smoothing-masking procedure excludes much, but not all, noise from the moment maps.

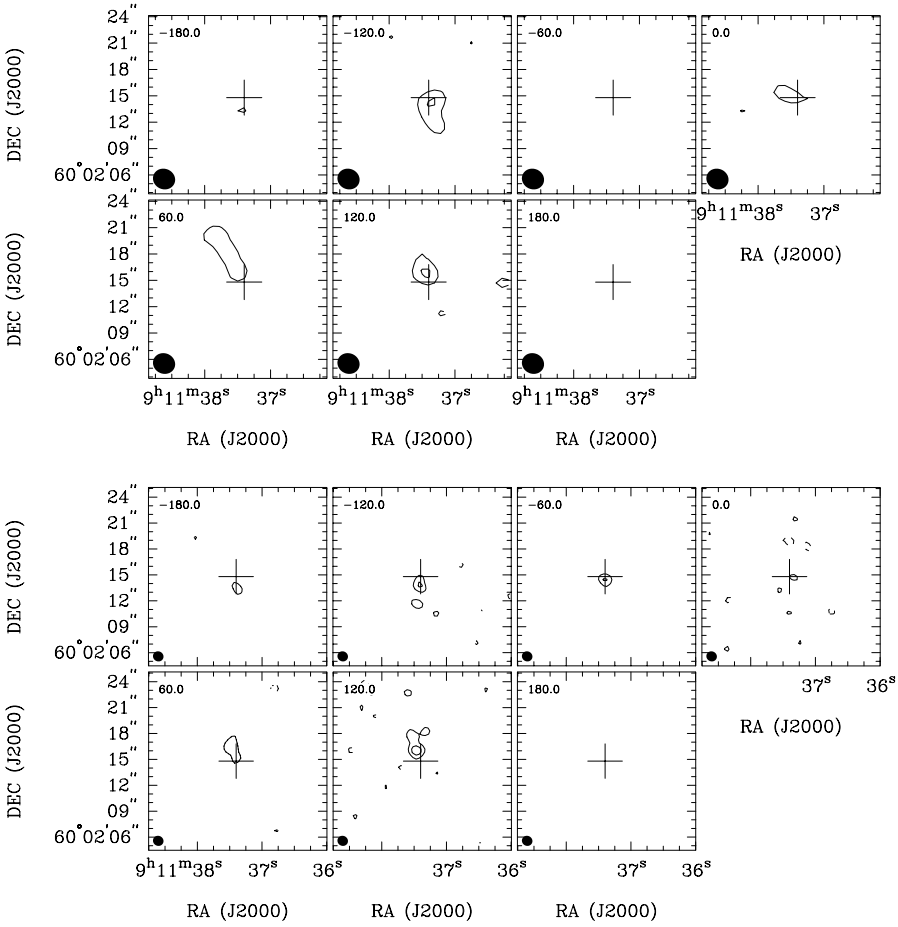

Figure 2. Channel maps of NGC 2768. Top panel: ^{12}CO(1–0) line. Bottom panel: ^{12}CO(2–1) line. The channels are 60 km s^{-1} wide and contours are plotted at −3 (dashed), 3, 6 and 9σ with $\sigma = 1.0$ mJy beam^{-1} for CO(1–0) and $\sigma = 1.6$ mJy beam^{-1} for CO(2–1). The number in the top left-hand corner of each frame is the central velocity of that frame, relative to the observed central velocity of $V_{\rm sys} = 1373$ km s^{-1}. The cleaned beam is shown in the bottom left-hand corner of each frame. The cross marks the centre of the 5 GHz radio continuum (Nagar et al. 2005).

As shown in the integrated intensity maps of both transitions, the CO is distributed somewhat asymmetrically, although with the signal just above 3σ in most of the velocity channels, we have to be wary of the contribution of noise even with the smoothing and masking procedure applied. The smaller CO(2–1) beam resolves two peaks in the CO intensity, one directly south of the galaxy centre and one to the north by north-east. The two clear CO(2–1) peaks suggest that the densest gas might be in a disc or ring seen nearly edge-on. The lower resolution CO(1–0) data blend these two separate peaks into one peak elongated in the direction of the CO(2–1) peaks. In addition, the CO(1–0) data pick up an extended structure along PA $\approx 30^{\circ}$, especially prominent to the north-east. While this feature is absent in the CO(2–1) maps, it appears in both the 40 and 80 km s^{-1} channels of the CO(1–0) data, suggesting it is not just noise. The CO(2–1) observations must miss this molecular gas through some combination of the more limited primary beam size, noise, and a potentially lower excitation temperature of the infalling gas. Overall, the molecular gas distribution suggests that we are observing the formation of an inner polar ring or disc, with gas in the outskirts of the inner kiloparsec still being accreted on to the settled structure.

The velocity maps (Fig. 3) and PV diagrams (Fig. 4) support this interpretation. The overlay of the CO(1–0) PV contours on the CO(2–1) PV pixel map in Fig. 4 shows that the rotation of the main body of molecular gas is in good agreement for the two lines. Unfortunately, the quality of the data does not allow us to reliably determine whether the molecular gas is in a ring or a disc. For simplicity and given the hint of a flattening of the rotation at offsets larger than ≈22 arcsec, we refer to it as a disc for the remainder of the paper but refrain from making any claims that depend on whether it is a disc or a ring. The polar rotation is consistent with the velocity field of the more extended ionized gas (Sarzi et al. 2006). However, the CO(1–0) mean velocity map is irregular in the northern part of the galaxy. This irregularity is caused by the lower velocity (40 and 80 km s^{-1}) molecular gas making up the extension to the north-east of the galaxy centre, as can be clearly seen in the CO(1–0) PV contours. The velocity and extent of this gas lead to the conclusion that it must not yet be a part of the central regularly rotating structure, but instead be in the process of accreting on to this structure. While other minor irregular features in the velocity maps may indicate further irregularities in the molecular gas kinematics, the accidental inclusion of a noise peak from a particular channel map could influence the velocity map in the same way, thus we hesitate to analyse these features.

To construct integrated spectra and determine total fluxes, we selected the pixels in the central non-zero parts of the two integrated intensity maps as our spatial regions of interest. Integrating the original data cubes over these spatial regions gave us the spectra shown in Fig. 5. Spectra from the 30-m single-dish observations of Combes et al. (2007) are overplotted in dotted lines.

Comparison with the Combes et al. (2007) 30-m data shows that the double-peaked profile seen in both lines in the interferometric data is absent in the 30-m single-dish data. While the large amount of noise in the 30-m spectra certainly contributes to the difference in the spectral profiles, we also note that both 30-m spectra are biased towards the positive relative velocities seen on the northern side of the galaxy. If the 30 m's pointing were off to the north, it would explain why intensity is preferentially missing at the negative velocities. However, the intensities at positive relative velocities at 1 mm are also much lower than found with the interferometer. This difference suggests that the pointing may have also been off in the east–west direction. The 1-mm spectrum suffered much more from

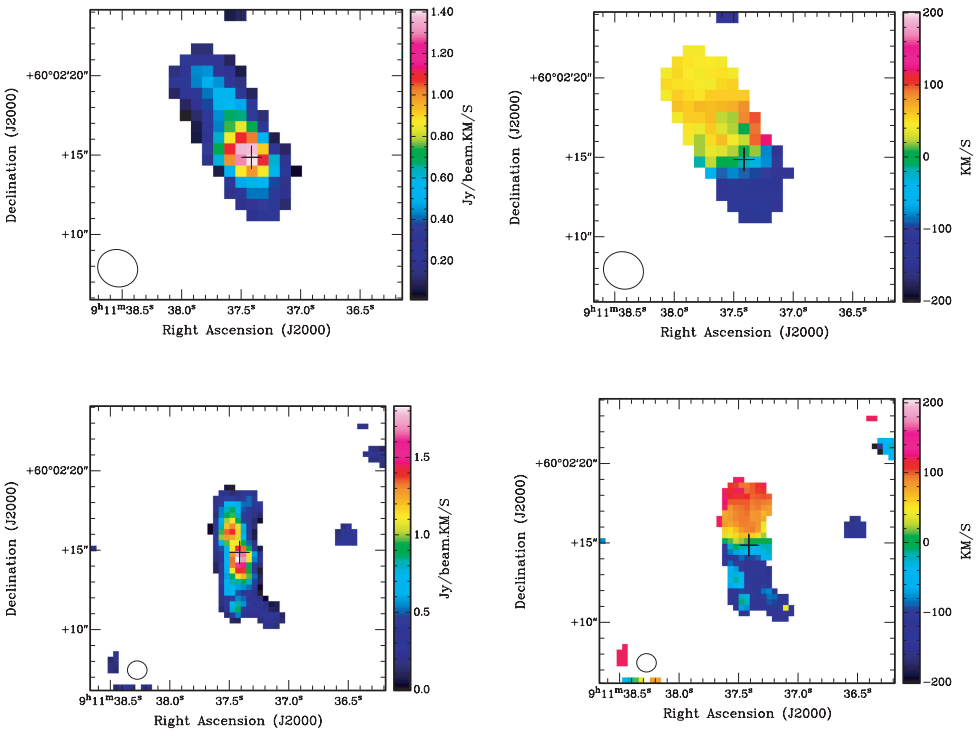

Figure 3. Left-hand panel: CO integrated intensity maps of NGC 2768. Right-hand panel: CO mean velocity maps. Top panel: CO(1–0). Bottom panel: CO(2–1). The synthesized beam is shown in the bottom left-hand corner of each map. The black cross marks the centre of the 5 GHz radio continuum (Nagar et al. 2005). White pixels have been masked according to the procedure described in Section 3.2.

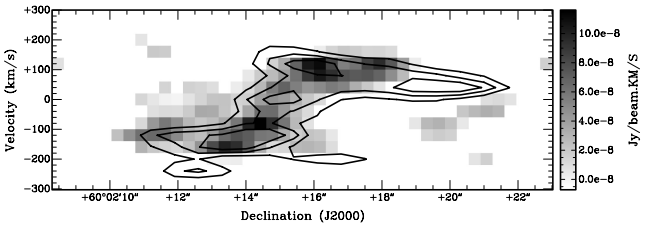

Figure 4. PV diagram of NGC 2768 along the polar axis. The pixels show the CO(2–1) emission, while the contours show the CO(1–0) emission at 3, 6 and 9 $\times$ 10^8 Jy beam^{-1} km s^{-1}. White pixels have been masked according to the procedure described in Section 3.2.

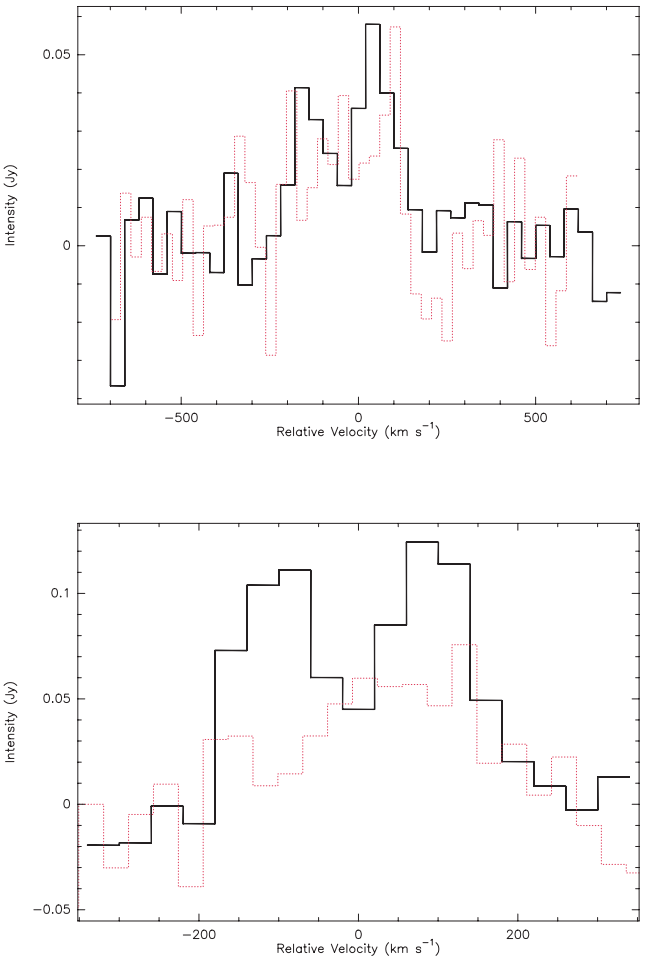

Figure 5. Solid lines show integrated spectra of the CO(1–0) line (top panel) and CO(2–1) line (bottom panel) in NGC 2768. The dotted lines show the single-dish spectra of Combes et al. (2007).

this pointing error as the half-power beamwidth is only 11 arcsec. We note that errors in the flux calibrations could also explain some of the discrepancy.

To estimate the total CO flux in each line, we integrated the spectra over the velocity range with observed emission, i.e. from 1193 to 1553 km s^{-1}. Table 2 reports the calculated total fluxes, 11.3 Jy km s^{-1} at CO(1–0) and 30.6 Jy km s^{-1} at CO(2–1). Fluxes for the 30 m observations of Combes et al. (2007) are also reported; these fluxes have been calculated over identical velocity ranges as their interferometric counterparts. For CO(1–0), the fluxes agree within the noise and the errors in the flux calibration. For the CO(2–1) line, the 30 m misses much of the flux seen by the interferometer, especially at negative relative velocities where the flux from the 30 m is 8.2 Jy km s^{-1} less than for the interferometer. As we have noted above, we believe much of this difference to be due to a pointing error.

Table 2. CO fluxes and molecular mass estimates in NGC 2768.

Line	Instrument	Flux (Jy km s^{-1})	M_{H_2} (10^7 M$_\odot$)
^{12}CO(1–0)	30 m	10.4 ± 1.6 ± 1.0	6.4 ± 1.0 ± 0.6
^{12}CO(1–0)	PdB	11.3 ± 1.3 ± 2.3	6.8 ± 0.8 ± 1.4
^{12}CO(2–1)	30 m	18.6 ± 2.5 ± 1.9	
^{12}CO(2–1)	PdB	30.6 ± 1.7 ± 6.1	

Errors reported are random and systematic (flux calibration) errors, respectively.

We used the total fluxes in CO(1–0) to compute the total molecular hydrogen mass using the formula $M(H_2) = (1.22 \times 10^4\,M_\odot)\,D^2\,S_{CO}$, where D is the distance measured in Mpc and S_{CO} is the total CO(1–0) flux. This formula comes from using the standard CO to H_2 conversion ratio $N(H_2)/I(CO) = 3 \times 10^{20}$ cm^{-2}, where $N(H_2)$ is the column density of H_2 and I(CO) is the CO(1–0) intensity in K km s^{-1}. The total H_2 mass detected by our interferometric observations is then 6.8 $\times$ 10^7 M$_\odot$. As nearly all the CO(1–0) flux comes from the nascent polar disc seen in the integrated intensity maps, this gives a rough estimate of the molecular mass already in the central polar disc. We estimate the integrated line ratio $R_{21} = CO(2–1)/CO(1–0) \approx 0.7$, indicating optically thick molecular gas that is subthermally excited, as expected for a non-starburst galaxy. This ratio is computed assuming we have mapped the full extent of the CO in both lines in our interferometric maps. As the CO distribution in both lines is only about half the diameter of the half-power beam width (HPBW) of the primary beam, this assumption is reasonable.

4 DISCUSSION

4.1 Origin of the molecular gas

With H I data from Morganti et al. (2006), dust maps from *Hubble Space Telescope* (*HST*) images (e.g. Fig. 6), and the molecular gas maps of Section 3, we now have a fairly complete census of the cool ISM in and around NGC 2768. The most striking feature, besides the fact that the ISM lies in the polar plane, is the clear link between all components. All observed phases of the cool ISM extend to the north-east, first in CO, then dust, then H I (Fig. 6). This shared asymmetry ranges from the inner kiloparsec in the molecular gas to over 30 kpc in H I. This link between the different ISM components clearly indicates that they were all accreted from the same source. It also suggests that the gas accretion will continue for some time, perhaps in discrete episodes.

This extended and asymmetric morphology along with the misaligned kinematics of the cool gas also firmly indicates an external origin. We consider three options: a minor merger with a gas-rich dwarf, tidal accretion from a gas-rich galaxy and accretion from an H I filament. The regularity of both the photometry and stellar kinematics of NGC 2768 argues against the recent merger of a gas-rich dwarf galaxy. Neither stellar tidal tail nor other irregularity has been observed, although the data we have access to do not pose particularly stringent upper limits (i.e. the optical photometry is relatively shallow). The accretion of primordial (metal free) H I scenario fails to explain both the dust and CO observed. We thus consider tidal accretion as the most likely scenario.

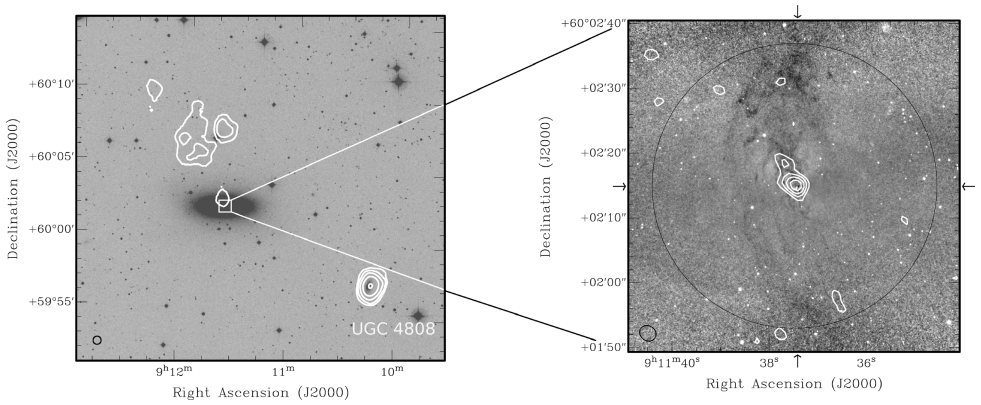

Figure 6. The cool ISM in NGC 2768. The left-hand panel shows the H I surface density distribution in contours of 2, 4, 8, 16 and 32 × 10^{19} atom cm^{-2} plotted over an *R*-band Digital Sky Survey (DSS) image. UGC 4808 is visible in the bottom right-hand corner. The right-hand panel shows the CO(1–0) intensity distribution in contours of 0.5, 0.75, 1.0 and 1.25 Jy km s^{-1} plotted over a dust map of NGC 2768 obtained by dividing the *HST* F814W ACS image by an ellipse model fit. In the right-hand panel, the outer circle indicates the 44 arcsec HPBW of the CO(1–0) primary beam of the interferometer and the arrows indicate the galaxy centre. The black ellipses in the bottom left-hand corners of both panels show the synthesized beams of the H I and CO observations, respectively.

The loose-group centred on NGC 2768, catalogued as Lyon Group of Galaxies (LGG) 167 (Garcia 1993), contains many potential gas-donor galaxies (see Table 3). The H I data cube obtained by Morganti et al. (2006) reveals neutral hydrogen around four lower luminosity galaxies within a 150 kpc projected separation from NGC 2768. The H I velocities indicate group membership for all of these galaxies. Considering the wide range (0.1 to 6) of H I mass to blue luminosity ratio ($M_{\rm H\,I}/L_{\rm B}$) values found in late-type dwarf galaxies (Swaters 1999), any of these galaxies could have provided the $\sim 10^8$ M$_\odot$ of H I found around NGC 2768 without requiring an unreasonable amount of H I for its blue luminosity.

Including all galaxies within 400 kpc in projected separation and 400 km s^{-1} in relative line-of-sight velocity from NGC 2768, we created a list of known galaxies that may have recently interacted with NGC 2768 (Table 3). Given the relaxed appearance of the ionized gas in the SAURON map (Sarzi et al. 2006), we estimate that this gas must have been present for at least 3–10 dynamical time-scales, or 0.2–0.7 Gyr. Assuming $\sigma_{\rm group} = 200$ km s^{-1} as a reasonable 3D velocity dispersion for a small group, we estimated the time since each galaxy could have interacted with NGC 2768:

$$\Delta t = \frac{\Delta R}{\sqrt{\sigma^2_{\rm group} - \Delta V^2_{\rm sys}}},$$

where ΔR is the projected separation and $\Delta V_{\rm sys}$ is the line-of-sight velocity relative to NGC 2768. Values of this estimated interaction time are listed in Table 3. This analysis shows that the nearby Scd galaxy UGC 4808 is most likely to have interacted with NGC 2768 recently and provided the cool ISM. UGC 4808 can be seen in the bottom right-hand corner of Fig. 6. Its alignment with the large-scale H I supports this conclusion.

4.2 Fate of the molecular gas: star formation?

In NGC 2768, we observe no definitive signs of young stars as seen in the other five SAURON early-type galaxies with mapped CO emission (NGC 2865, Schinnerer & Scoville 2002; NGC 3032, NGC 4150, NGC 4459 and NGC 4526, Young, Bureau & Cappellari

Table 3. Basic properties of galaxies near NGC 2768. This table lists all galaxies with a projected distance differing by less than 400 kpc and a redshift differing by less than 400 km s^{-1} from NGC 2768. Only galaxies with known redshifts are included.

Name	$\Delta\theta$	ΔR (kpc)	ΔV$_{\rm sys}$ (km s^{-1})	$B_{\rm T}$ (mag)	$M_{\rm H\,I}$ (10^8 M$_\odot$)	$M_{\rm H\,I}/L_B$ (M$_\odot$/L$_\odot$)	Δt (Gyr)	Type (NED)
(1)	(2)	(3)	(4)	(5)	(6)	(7)	(8)	(9)
NGC 2768	–	–	–	10.60	1.7	0.007	–	E
UGC 04808	11′.5	72	−78	15.03	1.6	0.41	0.38	Scd
PGC 025982	16′.5	103	−236	14.71				
MAILYAN 038	19′.8	124	187		0.3		1.71	
PGC 2599651	21′.8	136	197	17.05	0.4	0.63	3.83	
PGC 2601563	22′.5	141	−325	17.36	0.6	1.4		
SDSS J091531.98+594948.5	31′.9	200	−5	17.14			0.98	
NGC 2742	40′.2	252	−84	11.38	18.4	0.16	1.36	SA(s)c
NGC 2726	50′.6	317	145	12.56	1.8	0.05	2.25	Sa?

(1) Galaxy name. (2) Angular separation. (3) Projected separation (assuming a distance of 21.5 Mpc). (4) Relative line-of-sight velocity. (5) Total corrected apparent blue magnitude (HYPERLEDA). (6) Mass of neutral hydrogen (Morganti et al. 2006, except for NGC 2742 – Broeils & van Woerden 1994 and NGC 2726 – Haynes et al. 1988). (7) H I mass to total blue luminosity ratio. (8) Estimate for time since a possible interaction with NGC 2768. (9) Galaxy classification (NED).

2008). Excluding NGC 2685, in which the CO lies outside of the SAURON field of view, young stars in these galaxies are traced by high-Hβ line strengths (all), cold stellar components that share the CO kinematics (all except NGC 3032) and low [O III] to Hβ emission-line ratios (all except NGC 4150).

The Hβ line-strength index of NGC 2768 is 1.70 Å within a central 9 arcsec radius aperture (one-eighth of the effective radius) and remains near this level over the entire SAURON field (Kuntschner et al. 2006; fig. 7). Higher resolution but lower signal-to-noise ratio data from the OASIS integral-field spectrograph give slightly larger values for the Hβ line strength (McDermid et al. 2006). However, the discrepancy between the OASIS and SAURON values is probably attributable to the difficulty of subtracting the strong Hβ emission before fitting the line strengths, and the higher signal-to-noise ratio data from SAURON provide a better estimate. Combining line-strength indices (Hβ, Fe5015, and Mg*b*) with stellar population models, Kuntschner et al. (in preparation) show that NGC 2768 has a fairly uniform, old stellar population. However, line strengths are not sensitive to very recent star formation nor to a very small percentage of young stars superposed on a dominant older stellar population, so line strengths cannot rule out particularly recent and/or weak star formation.

The SAURON map of the stellar velocity dispersion shows a dramatic drop of $\approx$45 km s^{-1} in the innermost 8 arcsec (Emsellem et al. 2004; fig. 7). This drop in dispersion is also clearly seen in long-slit data (Simien & Prugniel 1997) and in OASIS data (McDermid et al. 2006). Young stars born from dynamically cold gas in a cicumnuclear disc can produce such a drop in dispersion (Emsellem et al. 2001; Wozniak et al. 2003), but they should also produce a notable effect in the velocity map. However, the velocity field of NGC 2768 lacks any signature of a dynamically cold stellar disc or ring. Thus, the stellar velocity dispersion drop cannot be directly attributed to the formation of a stellar component either from the molecular polar ring itself, or from gas settled into the main plane of the galaxy as may occur during polar accretion events (Bournaud & Combes 2003). Additionally, it is difficult to associate this drop to a young stellar population, as no coincident increase in Hβ line strength is observed. We conclude that no kinematic component visible in the SAURON maps is directly related to the molecular gas.

Particularly, low ratios of [O III] to Hβ [$\log([\mathrm{O\,III}]/\mathrm{H}\beta) < -0.2$] indicate star formation as the source of ionization (Ho, Filippenko & Sargent 1997). In NGC 2768, $\log([\mathrm{O\,III}]/\mathrm{H}\beta)$ ranges from about 0.0 to 0.5. In this range, the ionization can come from sources other than star formation. The four additional possibilities are heating by an X-ray halo, an AGN, shocks or post-asymptotic giant branch (post-AGB) stars. NGC 2768 lacks an X-ray halo (Komossa et al. 1999), so this option is ruled out. The Hβ flux in NGC 2768 does not drop off with the square of the radius as it should if ionized solely by an AGN (Hatch, Crawford & Fabian 2007), therefore everything outside the central 2 arcsec must be ionized by another source (Sarzi et al., in preparation).

The most prominent feature of the ionized gas in NGC 2768 is a roughly spiral-shaped region of increased [O III] equivalent width (see fig. 4b, Sarzi et al. 2006). This strong enhancement in [O III] without a corresponding strong enhancement in Hβ is seen in other SAURON galaxies (NGC 2974, NGC 3414) and must be caused by shock ionization of the gas, as post-AGB stars are too symmetric to cause such asymmetric ionization and star formation would not cause such an increase in [O III]. Yet the smooth and circular Hβ emission suggests that an ionization source other than shocks is responsible for the ionization outside of the spiral pattern. Both star formation and post-AGB stars remain options. Post-AGB stars must be present in such an old galaxy and thus must play a role. However, the Hβ equivalent width map from SAURON shows a weak enhancement along the extended molecular gas seen to the northeast of the galaxy centre (see Fig. 7), pointing to star formation in this ionized gas.

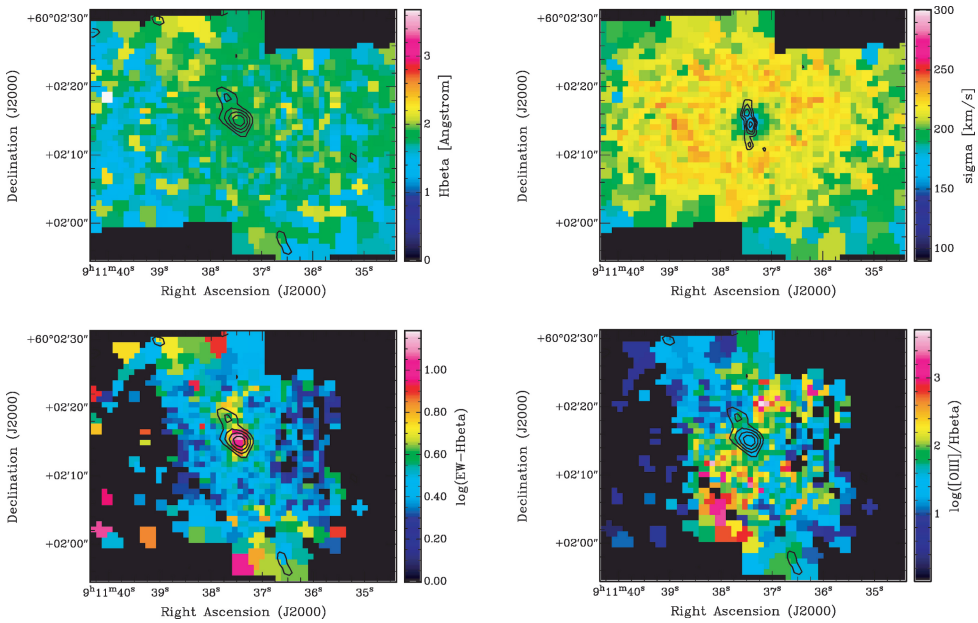

Figure 7. Top left-hand panel: CO(1–0) contours of NGC 2768 over the SAURON Hβ absorption line-strength map (Kuntschner et al. 2006). No significant change in line strength is coincident with the molecular gas. Top right-hand panel: CO(2–1) contours over the stellar velocity dispersion map (Emsellem et al. 2004). The CO is co-spatial with the dispersion drop. Bottom left-hand panel: CO(1–0) contours over a map of the equivalent width of Hβ emission (Sarzi et al. 2006). Note the increase in equivalent width near the extended CO peak to the north-east. Bottom right-hand panel: CO(1–0) contours over a map of the flux ratio of [O III] to Hβ emission (Sarzi et al. 2006).

The FIR luminosity ($L_{\rm FIR}$) to molecular mass ($M_{\rm H_2}$) ratio also provides possible evidence of star formation (Combes et al. 2007). We computed a bolometric FIR flux for NGC 2768:

$$\mathrm{FIR} \equiv 1.26 \times 10^{-14}\ \mathrm{W\,m^{-2}}(2.58\ S_{60\,\mu\mathrm{m}} + S_{100\,\mu\mathrm{m}}),$$

where $S_{60\,\mu\mathrm{m}}$ and $S_{100\,\mu\mathrm{m}}$ are IRAS fluxes in Jy. The total FIR luminosity is then $L_{\rm FIR} = (\mathrm{FIR})\,4\pi D^2 = 4.3 \times 10^8\ \mathrm{L_\odot}$, giving a $L_{\rm FIR}$ to $M_{\rm H_2}$ ratio of 6.3 $\mathrm{L_\odot/M_\odot}$, a reasonable value for a star-forming spiral (Devereux & Hameed 1997). In spiral galaxies, FIR emission traces star formation activity and the ratio of $L_{\rm FIR}$ to $M_{\rm H_2}$ is assumed to measure how efficiently stars are being formed out of the molecular hydrogen. If star formation is the dominant process contributing to FIR emission in NGC 2768, then star formation is proceeding at a normal efficiency. However, other sources (such as an AGN) may significantly contribute to the FIR emission in early-type galaxies, weakening this conclusion. We can still use the FIR luminosity to give an upper limit to the star formation rate, deriving an upper limit of 0.07 solar masses per year (Kennicutt 1998, equation 4). Thus, if star formation is present in NGC 2768, it is occurring at a very low rate and the time-scale to exhaust the supply of molecular gas is around 1 Gyr.

As we have only unclear evidence of ongoing star formation in NGC 2768, we consider whether the molecular gas disc might be gravitationally stable and thus unable to form stars. Theoretical models from Kawata, Cen & Ho (2007) suggest that circumnuclear discs in massive galaxies are more stable than those in less massive galaxies. A stability analysis of the molecular circumnuclear disc in 3C 31 based on Toomre's Q parameter (Toomre 1964) suggests that it is gravitationally stable and thus unable to form stars (Okuda et al. 2005). Our data are insufficient to calculate Toomre's Q parameter by themselves, but comparing with the models of Kawata et al. (2007) (see their fig. 5), we find that the 0.5 kpc radius and $6.8 \times 10^7\ \mathrm{M_\odot}$ mass of the molecular disc in NGC 2768 should be unstable, with a Q parameter less than 1. Thus, it is reasonable to expect star formation in the polar disc of NGC 2768.

4.3 Origin of the mm continuum

From radio and X-ray observations, we know that NGC 2768 is a low-luminosity AGN. VLA and Very Long Baseline Array (VLBA) observations indicate a compact radio source with no evidence of jets (Nagar et al. 2005). Most if not all X-ray emission are consistent with a point-source origin, and the X-ray count rate differed between observations a month apart, indicating that the X-ray source is variable (Komossa et al. 1999).

The few LLAGN that have been studied at mm frequencies show a range of spectral shapes attributed to varying contributions from optically thin synchrotron emission, self-absorbed synchrotron emission and free–free emission (see Nagar et al. 2002; Doi et al. 2005; Krips et al. 2007). In Fig. 8, we plot the radio through FIR spectral energy distribution of NGC 2768, which is similar to those of some of the other LLAGN previously observed. Values and references are listed in Table 4. We note that the flux densities at different frequencies are necessarily at different resolutions and thus are not entirely comparable. However, as no extended structures are observed at the milliarcsecond resolution of the VLBA at 5 GHz, and the 1.4, 15 and 115 GHz detections are all consistent with a point-source origin, we assume all these flux densities are dominated by an unresolved source and can thus be compared without correction. The upper limit at 230 GHz is also for a point source at the phase centre at the resolution of $1\farcs2 \times 1\farcs2$, while the 240 GHz detection is a bolometric measurement from an 11 arcsec beam, which could include a contribution from cold dust (Wiklind & Henkel 1995) as well as from a central AGN. These two observations are thus not as contradictory as they appear in the SED plot. However, we note that our map of 1-mm continuum emission does not trace the dust pattern seen in Fig. 6 nor do we see evidence of more emission in the central 11 arcsec after smoothing our data to this resolution.

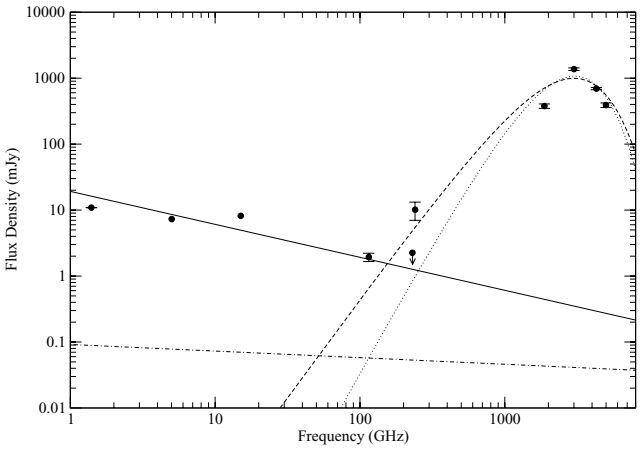

Figure 8. Spectral energy distribution of NGC 2768 from the radio to the far-infrared (FIR). The solid line is an $\alpha = -0.5$ power-law fit, modelling synchrotron emission. The dot–dashed line estimates the maximum contribution from free–free emission. The dashed curve extrapolates from the FIR dust bump to mm wavelengths using a $\beta = 1$ emissivity law; the dotted curves does the same with $\beta = 2$.

Table 4. Spectral energy distribution of NGC 2768.

Instrument	Frequency (GHz)	Flux density (mJy)	References
WRST	1.4	10.9	1
VLBA	5	7.3	2
VLA	15	8.2	2
PdB	115	1.94	3
PdB	230	< 2.25	3
IRAM 30 m	240	10.1	4
MIPS	1875	377	5
IRAS	3000	1370	6
MIPS	4286	694	5
IRAS	5000	390	6

References – (1) Morganti et al. (2006); (2) Nagar et al. (2005); (3) this paper; (4) Wiklind & Henkel (1995); (5) Temi, Brighenti & Matthews (2007); (6) Moshir et al. (1990).

First, the lack of strong, coincident 1-mm continuum emission rules out cold dust as the origin of the 3-mm continuum emission, as the thermal spectrum from dust drops sharply towards mm wavelengths (see the dust curves in Fig. 8). We can also rule out free–free emission using the formula in Doi et al. (2005) which assumes an electron temperature of 10^4 K and $\mathrm{N(He^+)/N(H^+)} = 0.08$:

$$\left(\frac{S_\nu}{\mathrm{mJy}}\right) \approx 3.57 \times 10^{12} \left[\frac{F(\mathrm{H}\beta)}{\mathrm{erg\,cm^{-2}\,s^{-1}}}\right] \left(\frac{\nu}{\mathrm{GHz}}\right)^{-0.1}.$$

We use the total flux in Hβ from the SAURON data (Sarzi et al. 2006), which gives an overestimate for the central radio emission, as most of the Hβ emission comes from ionizing sources other than star formation and only the flux in the central pixels should correspond to H II regions that could appear as a central radio point source.

Nevertheless, Fig. 8 reveals that, even with this overestimate, free–free emission is far too faint to account for the 3-mm continuum.

Having ruled out dust and free–free emission, processes directly related with an accreting supermassive black hole are likely to be the source of the 3-mm continuum detected in NGC 2768. Optically thin synchrotron emission from compact jets or other ejecta will produce a spectrum with a spectral index of $\alpha \leq -0.5$. The logarithmic least-squares fit of an $\alpha = -0.5$ power law is shown in Fig. 8. It roughly fits the three radio data points and the 3-mm continuum emission, but the low value at 1.4 GHz and the high value at 15 GHz hint at a flatter or inverted spectrum, suggesting synchrotron self-absorption plays a role.

5 CONCLUSIONS

The interferometric observations of the CO(1–0) and CO(2–1) lines presented here reveal a kiloparsec polar ring or disc of molecular gas within the early-type galaxy NGC 2768. This molecular gas reveals the potential of this galaxy to form kinematic substructure through star formation. However, neither the kinematics nor the line strengths of NGC 2768 as measured by SAURON show clear evidence of a young stellar population. This limits any star formation coincident with the molecular gas to be very recent and/or too small a luminosity-weighted fraction of the background old stellar population to contribute to the line strengths and kinematics. The asymmetric and unrelaxed nature of the CO(1–0) emission suggests that the molecular gas in NGC 2768 was recently accreted and is possibly still being accreted, in agreement with the much more extended but disturbed H I distribution. Searching the neighbourhood of NGC 2768 for potential gas-donor galaxies, many H I-rich low-luminosity galaxies are found, all of which could be the source of H I seen in and around NGC 2768, although UGC 4808 seems the most likely, being closest in projected distance and aligned with the extended H I distribution.

These CO observations of NGC 2768 probe new regions of parameter space in terms of molecular gas in early-type galaxies, with recently accreted, polar-rotating gas of only 6.8×10^7 $M_\odot$. As surveys have indicated lower CO detection rates in higher luminosity E and S0 galaxies (Lees et al. 1991; Sage, Welch & Young 2007), NGC 2768 is also notable for being the brightest in *B* band of the CO detections in Combes et al. (2007). Whether the lack of observed star formation has to do with the (short) time since the gas has been accreted, the (low) mass of molecular gas available for star formation, the polar dynamics of the gas, or some host-galaxy property will take more investigation to discover, including an analysis of the molecular gas distributions of other early-type galaxies with integral-field data.

ACKNOWLEDGMENTS

We would like to thank Philippe Salome for help with the reduction of the Plateau de Bure data and Marc Sarzi for useful discussions. We are also grateful to the SAURON Team for providing SAURON data as well as Tom Oosterloo for providing the H I data cube of NGC 2768. LMY acknowledges support from grant NSF AST-0507432 and would like to thank the Oxford Astrophysics Department for its hospitality during sabbatical work. We would also like to thank the anonymous referee for helpful comments which improved the paper.

The dust maps used observations made with the NASA/ESA *Hubble Space Telescope*, obtained from the data archive at the Space Telescope Institute. STScI is operated by the association of Universities for Research in Astronomy, Inc. under the NASA contract NAS 5-26555. The NASA/IPAC Extragalactic Data base (NED) is operated by the Jet Propulsion Laboratory, California Institute of Technology, under contract with the National Aeronautics and Space Administration. This research made use of HYPERLEDA: http://leda.univ-lyon1.fr. The Digitized Sky Surveys were produced at the Space Telescope Science Institute under US Government grant NAG W-2166. The images of these surveys are based on photographic data obtained using the Oschin Schmidt Telescope on Palomar Mountain and the UK Schmidt Telescope.

REFERENCES

Bournaud F., Combes F., 2003, A&A, 401, 817
Broeils A. H., van Woerden H., 1994, A&AS, 107, 129
Combes F., Young L. M., Bureau M., 2007, MNRAS, 377, 1795
de Vaucouleurs G., de Vaucouleurs A., Corwin H. G., Buta R. J., Paturel G., Fouque P., 1991, Third Reference Catalog of Bright Galaxies, Vols. 1–3, XII. Springer-Verlag, Berlin (RC3)
de Zeeuw T. et al., 2002, MNRAS, 329, 513
Devereux N. A., Hameed S., 1997, ApJ, 113, 599
Djorgovski S., Davis M., 1987, ApJ, 313, 59
Doi A., Kameno S., Kohno K., Nakanishi K., Inoue M., 2005, MNRAS, 363, 692
Dressler A., Lynden-Bell D., Burstein D., Davies R. L., Faber S. M., Terlevich R., Wegner G., 1987, ApJ, 313, 42
Emsellem E., Greusard D., Combes F., Friedl D., Leon S., Pécontal E., Wozniak H., 2001, A&A, 368, 52
Emsellem E. et al., 2004, MNRAS, 352, 721
Emsellem E. et al., 2007, MNRAS, 379, 401
Garcia A. M., 1993, A&AS, 100, 47
Guilloteau S., Lucas R., 2000, in Mangum J. G., Radford S. J. E., eds, ASP Conf. Ser. Vol. 217, Imaging at Radio through Submillimeter Wavelengths. Astron. Soc. Pac., San Francisco, p. 299
Hatch N. A., Crawford C. S., Fabian A. C., 2007, MNRAS, 380, 33
Haynes M. P., Magri C., Giovanelli R., Starosta B. M., 1988, AJ, 95, 607
Heckman T. M., 1980, A&A, 87, 152
Högbom J. A., 1974, A&AS, 15, 417
Ho L. C., Filippenko A. V., Sargent W. L., 1997, ApJS, 98, 477
Jesseit R., Naab T., Peletier R. F., Burkert A., 2007, MNRAS, 376, 997
Kawata D., Cen R., Ho L. C., 2007, ApJ, 669, 232
Kennicutt R. C. Jr., 1998, ARA&A, 36, 189
Kim D., 1989, ApJ, 346, 653
Knapp G. R., Guhathakurta P., Kim D., Jura M. A., 1989, ApJS, 70, 329
Komossa S., Böhringer H., Huchra J. P., 1999, A&A, 349, 88
Krips M. et al., 2007, A&A, 464, 553
Kuntschner H. et al., 2006, MNRAS, 369, 497
Lees J., Knapp G. R., Rupen M. P., Phillips T. G., 1991, ApJ, 379, 177
McDermid R. M. et al., 2006, MNRAS, 373, 906
Morganti R. et al., 2006, MNRAS, 371, 157
Moshir M. et al., 1990, IRAS Faint Source Catalog, version 2.0
Nagar N. M., Wilson A. S., Falcke H., Ulvestad J. S., Mundell C. G., 2002, in Maiolino R., Marconi A., Nagar N., eds, ASP Conf. Ser. Vol. 258, Issues in Unification of Active Galactic Nuclei. Astron. Soc. Pac., San Francisco, p. 171
Nagar N. M., Falcke H., Wilson A. S., 2005, A&A, 435, 521
Okuda T., Kohno K., Iguchi S., Nakanishi K., 2005, ApJ, 620, 673
Sage L. J., Welch G. A., 2006, ApJ, 644, 850
Sage L. J., Welch G. A., Young L. M., 2007, ApJ, 657, 232
Sandage A., Bedke J., 1994, The Carnegie Atlas of Galaxies. Carnegie Institute of Washington with The Flintridge Foundation, Washington, DC
Sarzi M. et al., 2006, MNRAS, 366, 1151
Sault R. J., Teuben P. J., Wright M. C. H., 1995, in Shaw R. A., Payne H. E., Haynes J. J. E., eds, ASP Conf. Ser. Vol. 77, Astronomical Data Analysis Software & Systems IV. Astron. Soc. Pac., San Francisco, p. 433
Schinnerer E., Scoville N., 2002, ApJ, 577, L103

Simien F., Prugniel P., 1997, A&AS, 126, 519
Swaters R., 1999, PhD thesis, Rijksuniversiteit Groningen
Temi P., Brighenti F., Matthews W. G., 2007, ApJ, 660, 1215
Toomre A., 1964, ApJ, 139, 1217
Wiklind T., Henkel C., 1995, A&A, 297, L71
Wozniak H., Combes F., Emsellem E., Friedli D., 2003, A&A, 409, 469
Young L. M., 2002, ApJ, 124, 788
Young L. M., 2005, ApJ, 634, 258
Young L. M., Bureau M., Cappellari M., 2008, ApJ, 676, 317

This paper has been typeset from a TEX/LATEX file prepared by the author.